On the influence of specimen size and geometry on the fracture toughness of tungsten heavy metal alloys

M.E. Alam, G.R. Odette*

Materials Department, University of California, Santa Barbara, CA 93106, USA

A B S T R A C T

We previously showed that commercial tungsten (W)-based heavy metal alloy (WHA) composites containing 90 to 97 wt% W, reinforced with 3 to 10 wt% of a NiFe ductile phase (DP), have room temperature (RT) maximum load elastic-plastic fracture toughness (K_{Jm}) values from 69 to 110 MPa$\sqrt{m}$. This is far higher than for monolithic RT W toughness ($\approx 8 \pm 4$ MPa$\sqrt{m}$). In all cases, fracture took place by stable crack growth. However, these results were based on very small (16/3.3/1.65 mm) pre-cracked bend bar tests, which naturally raises the question of size effects on the measured K_{Jm}. While they are best thought of as being composites, here we experimentally assess size and geometry effects on the K_{Jm} of WHA, in the broad context of validity criteria that have been developed for both cleavage and ductile tearing, R-curve fracture in steels. Specifically, we examine the relation between K_{Jm} and a dimensionless elastic-plastic zone small scale yielding deformation limit criterion, $M \geq \sigma_o b_o/J_m$. Here σ_o is the flow stress, J_m is the measured J at maximum load, and b_o is the initial unbroken ligament dimension. Tests on specimens from 3x to 8x larger than the original small (1x) bend bars show only weak or no size effect up to 95W with $K_{Jm} \approx 82 \pm 5$ MPa$\sqrt{m}$. However, 3x 97W alloy fractured elastically at $K_{Im} \approx 38 \pm 4$ MPa$\sqrt{m}$. The corresponding average for the 1x specimens was K_{Jm} 100 $\pm$ 15 MPa$\sqrt{m}$ for the 90–95W and 69 $\pm$ 12 MPa$\sqrt{m}$ for the 97W alloys. The approximately constant K_{Jm} for 3–8x specimen sizes suggests that the M required for constraint-related size independence is ≈ 200. However, DP fraction also plays a role, and there are additional effects of compact tension versus bend bar specimen geometries.

© 2022 The Authors. Published by Elsevier B.V.

1. Introduction

Tungsten's (W) remarkable combination of high melting temperature, strength, thermal conductivity, and low sputtering rates make it the leading candidate for the plasma-facing fusion reactor components [1–4]. Unfortunately, intrinsically high brittle to ductile transition temperatures, coupled with low toughness and tensile ductility, which are further degraded by neutron irradiation, may limit the use of monolithic W as a structural material for fusion applications [1–8]. Fortunately, the introduction of small amounts of a ductile phase (DP) can increase the toughness of brittle matrix materials [9–12], in this case W heavy alloys (WHA). Such ductile phase toughening (DPT), in the WHA studied here, was provided by embedding brittle W-particles in a Ni-Fe-W ductile solid solution honeycomb [13–29].

The advantages and open questions about WHA related to fusion service are described elsewhere [25,30–35]; and WHA fabrica-

tion routes and basic properties are the subjects of extensive literature [20,26–28,32,36,37]. The dominant limiting mechanical property for W and W-alloys is often low fracture toughness [3,7,8,38]. Fracture toughness is likely to be especially important for fusion divertor applications, with high and cyclic thermal loads, often result in the formation of many sharp surface cracks in W divertors [1,2,39,40]. However, there are only a few papers in the literature reporting pre-cracked fracture toughness data on WHAs [19,30,32].

Classical ductile phase toughening is primarily due to bridging in the wake of a *macrocrack*, propagating in a brittle matrix, and other mechanisms such as crack arrest-re-nucleation-deflection [9,11]. However, in the case of the WNiFe WHA, toughening is dominated by *microcrack* arrest, blunting, and bridging in a fully ductilized crack tip fracture plastic process zone, as shown below in Fig. 1, and in Ref. [30]. Process zone deformation, including the embedded W particles, and dilatational effects of microcrack blunting, dissipate large amounts of energy. Further, the process-zone dilatation shields (lowers) the crack tip stress fields, suppressing primary crack propagation [30,41,42]. Notably, shielding by plastic microcrack blunting is far more effective in WHA

Nomenclature and Acronyms

A_p	Plastic area under the load-displacement curve
a	Crack length
a_i	Initial crack length
a_f	Final crack length
B	Specimen thickness
b_o	Initial unbroken ligaments
d	Load point displacement
d_m	Load point displacement at maximum load
$d_{0.8}$	Load point displacement at 80% of post-maximum load
E	Elastic modulus
E'	$= E/(1-\nu^2)$
J	J-integral energy release rate
J_c	Critical J at fracture
J_e	Elastic component of J
J_p	Plastic component of J
J_m	Measured total $J = J_e + J_p$ at maximum load
J_{lim}	Elastic-plastic J censoring limit for a specified M (see below)
K_{Im}	Measured elastic fracture toughness at maximum load $= \sqrt{(E'J_e)} = \sqrt{[J_e E/(1-\nu^2)]}$
K_{Jc}	Elastic-plastic fracture toughness
K_{Jlim}	ASTM E1921 standard K_{Jm} censoring limit for a specified $M = 30$ (see below)
K_{Jm}	Measured elastic-plastic fracture toughness at maximum load $= \sqrt{(E'J_m)}$
K_{Jp}	Maximum load plastic J contribution to K_{Jm}
M	$M = \sigma_o b_o /J$ is a plastic deformation factor related to deviations from small scale yielding fields, which affect the measured K_{Jm} when below an observed limit
P	Load
P_m	Maximum load
P_o	General yield limit load
S	Span
T_o	Master curve reference temperature
σ_o	Flow stress
σ_y	Yield stress
ν	Poisson's ratio
η	Dimensionless parameter to calculate limit load for CT specimens
3PB	Three-point bend specimen
BDTT	Brittle-to ductile transition temperature
CT	Compact tension specimen
CTOD	Crack tip opening displacement
DP	Ductile phase
DP_f	Measured DP surface area fraction
DR	Ductile rupture
EDM	Electrical discharge machining
EDS	Energy dispersive spectroscopy
LIM	Line intercept method
RT	Room temperature
SEM	Scanning electron microscopy
SSY	Small scale yielding
W	Tungsten
WC	Tungsten particle cleavage
WD	Tungsten-DP decohesion
WW	Tungsten particle-particle fracture
WHA	Tungsten heavy alloy

than that provided by elastic microcracks in brittle matrix systems [41,43,44]. These mechanisms lead to the ductilization of the en-

tire W-NiFe biphasic microstructure resulting in significant crack tip opening displacement (CTOD) ductility, and the corresponding development of large, classical plastic zones.

Self-similar small scale yielding (SSY) crack tip stress fields peak at 3–5 times the yield stress (σ_y) depending on the alloy strain hardening, at a distance of $\approx$ 2 CTOD distances ahead of a blunting crack [45]. In steels, cleavage occurs when the local fields exceed a critical stress which encompass a critical volume of material in front of the crack tip [46–48]. Reaching the K_{Jc} for the critical stress-volume condition triggers a propagating cleavage crack. Note, this local fracture process can also be described in terms of the weakest link (Weibull) statistics [45,48]. An alternative fracture mechanism in steels, is ductile crack growth (tearing) when the macrocrack sequentially coalesces with microvoids, which are formed on decohered particles, and grown by accumualtion of strain in the process zone of the propagating crack.

In contrast, crack propagation in WHA involves the formtion of W-particle microcracks in the process zone. The W-microcrack formation primarily involves both W cleavage (WC) and W particle-particle boundary fracture (WW). While not a dominant mechanism, W-DP decohesion (WD) can also form process zone microvoids [30]. Ductile rupture (DR) of the DP ligaments surrounding arrested W-particles eventually results in the microcrack coalescence. Thus, on a meso-macro scale, the RT fracture of the W-NiFe WHA somewhat resembles fracture behavior observed in steels for either: (a) intergranular fracture (WW); or, (b) quasi cleavage (WC), see Fig. 1, Supplemental Fig. SF-5 and Section 3.2 below. Given some similarities of the fracture processes, it follows that, with appropriate modifications, the deformation limits that define self-similar SSY fields, and other validity criteria in steels, might be applicable to WHA.

In our previous study [30], we measured the elastic-plastic maximum load fracture toughness (K_{Jm}) of four 90–97W-NiFe WHAs from RT down to liquid nitrogen temperature (-196 °C), using fatigue pre-cracked bend bars. The ASTM E1921 test standard procedure was used to evaluate the maximum load toughness, K_{Jm} [49]. Reasons for using some ASTM E1921 K_{Jm} procedures are explained later in this section, and in Section 2.2. The WHA alloys in these tests were shown to have much higher RT toughness ($\approx$ 9–13 times) and much lower brittle to ductile transition temperatures (BDTT -150 °C for 90W to -25 °C for 97W) compared to monolithic W (typically, several hundred °C) [5,30,50].

However, these results were based on tests using small bend bars with dimensions of $B \approx$ 1.65 mm thickness, b_o = 1.65–2.1 mm ligament, W = 2B width and, S = 4 W span. We will henceforth refer to these as being 1x specimens [30]. Due to the high yield strength and elastic moduli of the WHA, the tests were *nominally* consistent with the ASTM E1921 K_{Jc}- based censoring criterion for avoiding SSY constraint loss effects in steels on establishing the master curve reference temperature (T_o) at 100 MPa√m. However, the very small specimen dimensions naturally raise the questions about size effects [47,48,51,52]. Further, the E1921 K_{Jc}-based constraint limit for steels is not appropriate for WHA due to elastic modulus differences (see below).

Size and geometry effects in steels on cleavage fracture arise from: (a) triaxial constraint loss beyond SSY deformation limit, which lowers the high blunting crack tip stress fields; and, (b) weakest link statistical effects in highly stressed near tip volumes, associated with differences in the crack front length. Singly, and in combination, these mechanisms can result in a decrease in the measured cleavage K_{Jm} with increasing specimen, or cracked body size. Ductile tearing fracture may also be affected by the lower stress triaxiality on microvoid growth in small specimens beyond SSY deformation limits [53]. And, in the limit, the ductile failure (not formally fracture as governed by fracture toughness) may occur at net section stress limits for massive crack tearing and spec-
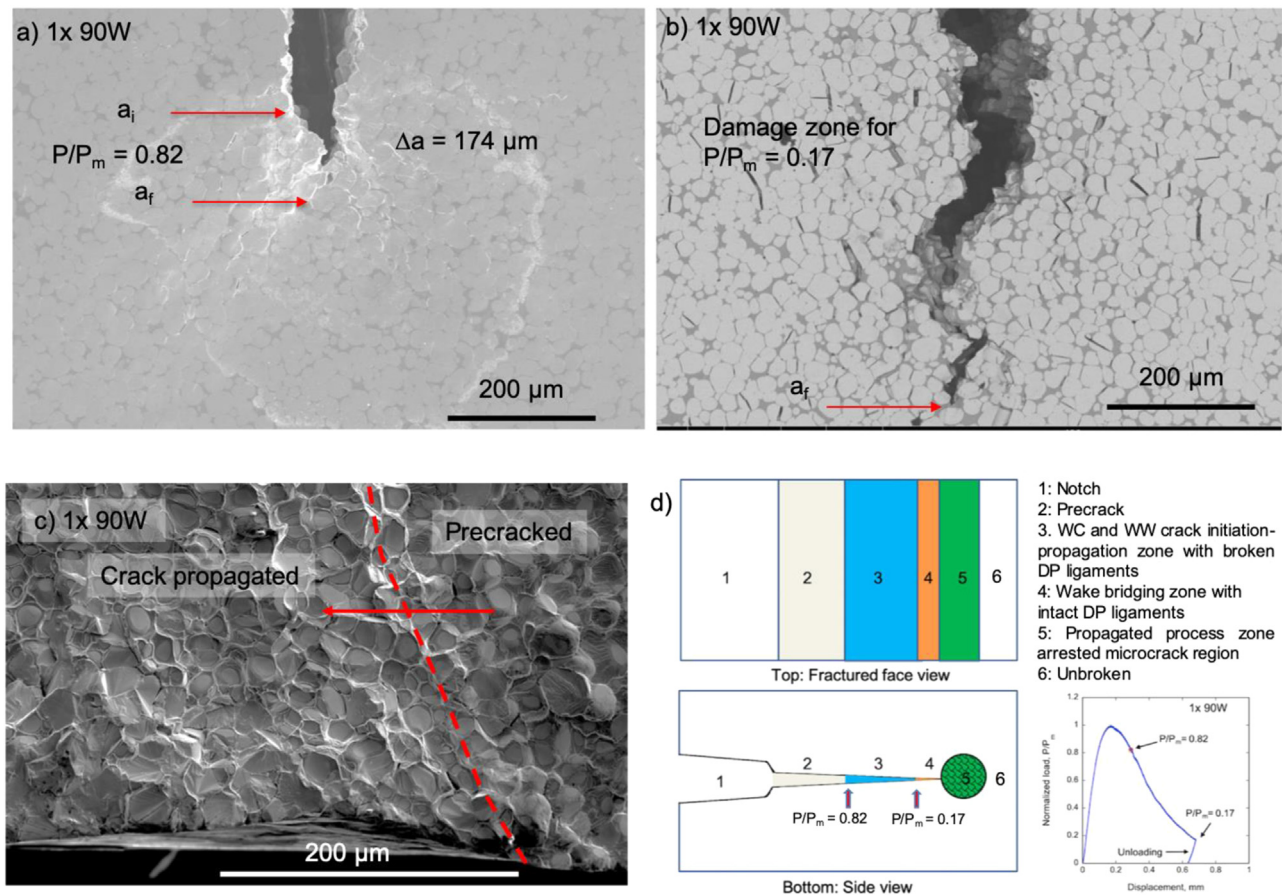
Fig. 1. (a and b) SEM images showing side surface of the process zone for a RT $1\times$ 90W with blunting down to $P/P_m \approx 0.82$ (a), and, stable crack propagation down to $P/P_m \approx 0.17$ (b); (c) SEM image of the fracture surface, near the precrack front, showing WC and WW domination of crack extension; and, (d) top and side view schematics illustration of the various crack propagation regions in WHA and a corresponding normalized load P/P_m– d curve.

imen hinging [45]. Here, we probe the effect of specimen size on the measured K_{Jm} for RT tests of specimens that are 3, 6, and 8 times (3x, 6x, and 8x) larger than the small (1x) bend bars. We also tested a compact tension (CT) specimens with a $B \approx 5.5$ times (5.5x) that of the 1x bend bar.

It is important to emphasize the objective of this paper. WHA are not steels, nor even standard metallic alloys. Rather, they are effectively biphasic composites. WHA fracture at RT is totally dominated by brittle W cleavage (WC) and W-W particle (WW) intergranular fracture, as modified by the presence of the surrounding ductile ligament phase, shown in Fig. 1a and b. Stable crack growth can occur in WHA due to the presence of the ductile phase, in the sense that the load (P) gradually decreases following the peak (Fig. 1b), partially in association with crack extension. However, the initial reduction in load occurs along a blunting line, with limited initial macro-fatigue crack extension of $< \sim 0.2$ mm. The load decreases because blunting is accompanied by extensive distributed arrested microcrack softening in the process zone ahead of the crack (Fig. 1a). The post maximum blunting line softening mechanism continues down to $P/P_m < 0.8$ (Fig. 1b). Larger subsequent load reductions may occur during crack growth due to macrocrack bridging by the ductile phase in the crack wake and continues process zone microcracking, as shown in Fig. 1b. However, in all cases the local fracture process is dominantly brittle, again mostly by WC and WW microcracking, as shown in Fig. 1b and c. In this sense, the WHA WC fracture process is somewhat akin to quasi cleavage, except that the rupture is in the ductile Ni-Fe-W ligaments, rather than shear zones between out-of-plane cleavage facets.

It is also important to emphasize that the extent of stable crack growth is mediated by complicated criteria, involving the loading compliance (including the specimen) versus the composite's R curve properties. The issue of crack growth stability becomes even more complex in cases with large-scale, crack-wake bridging by the ductile phase ligaments. A very simplified schematic of these toughening mechanism along with P/P_m – d curve is shown in Fig. 1d. Dealing with these crack growth stability complications is beyond the scope of this paper.

Various criteria have been used to specify the SSY deformation limits in steels. The most relevant is the ASTM Standard E1921 ASTM Master Curve Standard Practice "T_o" for determining the elastic-plastic K_{Jc} fracture toughness of steels in the cleavage transition. ASTM E1921 specifies a deformation limit (K_{Jlim}) for uncensored data used to determine the master curve 100 MPa√m reference temperature, T_o. The limit is given by

$$K_{Jlim} = \sqrt{[b_o \sigma_y E'/M]}$$
$$E' = E/[1 - \nu^2]$$
$$M = 30$$

Here, E is the elastic modulus, and ν is Poisson's ratio. However, the deformation limit should actually be expressed in terms of the elastic-plastic J-integral at fracture (J_{lim}), as

$$J_{lim} = b_o \sigma_o / M.$$

Thus, E' does not affect the J-based deformation limit. The E' values, needed to convert J_m to K_{Jm}, are ~ 232 GPa for steels, versus the average of ~ 432 GPa for 90–97% W WHA. The E1921 censoring is $M = 30$, but accounting for differences in the E',

the equivalent M for WHA is $30(E'_{WHA}/E'_{steel}) \sim 56$. However, the E1921 deformation limit of 30 for steels is known to be far too permissive, and a *M* value ($\geq$ 100–200) was found to be needed to fully avoid constraint loss effects in bend bar tests of steels [47,48,51,54].

In summary, we fully recognize that the use of ASTM E1921 standard for steels is not be strictly applicable to WHA. However, we did not use E1921 to try to determine a master curve T_o. Rather, we used the E1921's K_{Jm} evaluation procedures and as a basis for comparison of possible constraint limits and statistical effects in WHA versus those in steels. Our goal is to see how the behavior of WHA compares and/or contrasts to that observed in steels for size and geometry effects including the constraint limit deviations from SSY as referenced to E1921.

This paper is organized as follows. Following a Materials and Methods Section, the Results Section summarizes the effects of the specimen size on: the load-displacement curves and the corresponding maximum load elastic-plastic K_{Jm} values WHA with various DP contents. Note, we define an elastic K_{Im}, if the maximum load occurs on the elastic loading line, accompanied by unstable crack propagation, even if the test does not meet the formal size requirements of ASTM E399. A Discussion Section summarizes specimen size and geometry effects for the maximum load plastic K_{Jp}, the elastic K_{Im}, and total K_{Jm} values as a function of $\sigma_o b_o/J_m$, where, $J_m = J_p + J_e$.

2. Materials and methods

2.1. Materials

Four commercial (Mi-Tech Metals, Indianapolis, IN, USA) liquid-phase sintered (LPS) WHAs were received in the form of 100 mm x 100 mm x 14 mm plates. These WHA plates nominally contained 90, 92.5, 95, and 97W (wt%) with a DP balance of an initially 70% Ni and 30% Fe. The DP is enriched with W during the liquid phase sintering to form a fcc solid solution composition of $\approx$ 50% Ni, 30% W, and 20% Fe (wt%). The NiWFe phase forms a semi-continuous (mostly) thin-walled honeycomb web structure surrounding the much larger volume fraction of W-particles.

2.2. Characterization

The WHA specimens were fabricated by electrical discharge machining (EDM), ground with 220–2000 grit sand paper to remove EDM damage and residual surface stresses, selectively polished down with 0.5μ-diamond paste, and finally etched in a 30% hydrogen peroxide solution for 10 min to facilitate microstructural characterization. Scanning electron microscopy (SEM) with energy dispersive spectroscopy (EDS) was used to image the W particles and the surrounding ductile phase, and to identify their respective compositions. The W particle size distribution was determined by sampling $\sim$ 500 individual grains using 'ImageJ64' software. The W particle size increases from 17 $\pm$ 7 μm for 90W to 38 $\pm$ 15 μm for 97W [30]. The DP corresponding area fraction decreases from $\approx$ 16 $\pm$ 4% for 90W to $\approx$ 6 $\pm$ 2% for 97W, which was measured by converting the SEM BSE micrographs into binary black-white images to identify the associated DP area fractions (reported in %). The DP ligament thickness ($\approx$ 5 $\pm$ 5 μm for all WHAs) was measured by the line-intercept method (LIM) [30]. A detailed description of the characterization techniques can be found elsewhere [16,30].

Room temperature (RT) fracture toughness tests were conducted on three-point bend bars with length, width and thickness of: small 1x $\approx$ 16/3.3/1.65 mm, 3x $\approx$ 50/10/5 mm, 6x $\approx$ 90/20/10 mm, and 8x $\approx$ 110/25.4/12.7 mm dimensions. The specimens were fatigue pre-cracked to nominal crack length

(a)-to width (W) ratio, (a/W) $\approx$ 0.40–0.50 at a maximum ΔK_I = 15 MPa$\sqrt{m}$ and a load ratio, R = 0.1. The specimens were heat-tinted at 400 °C for 1–7 min, depending on specimen thickness. Three-point bend (3PB) tests with a span to width (S/W) ratio of $\approx$ 4 were carried out on an MTS 810 servo-hydraulic universal testing machine. The slightly modified 0.35T-CT (length x width x thickness $\approx$ 20/19/9 mm) specimens were fabricated from the tested 6x large 95W 3PB bars halves. The CT specimens were also fatigue precracked to a/W $\approx$ 0.45 following the similar precracking procedures to 3PB bars. The detailed CT geometry tested for this study can be found elsewhere [55].

The load (P) and load-point displacements (d) were measured and the K_{Jm} are defined at the maximum load (P_m) based on the ASTM E1921 standard practice method of estimating the J-integral elastic-plastic fracture toughness: $J_m = J_e + J_p$, as $K_{Jm} = \sqrt{\{J_m E/(1-\nu^2)\}}$; $J_e = K_{Im}^2(1-\nu^2)/E$, where K_{Im} is the elastic stress intensity factor at maximum load; and $J_p = 2A_P/Bb_o$ [49], B is specimen thickness, b_o is the initial unbroken ligament dimension, and A_P is the plastic area under the load-displacement curve [45,49,56]. It is also of interest to compare normalized P/P_o-d curves by dividing P by the plane strain limit load P_o. The 3PB bar plane strain limit load $P_o = 1.455Bb_o^2\sigma_o/S$, while for CT specimens, $P_o = 1.455\eta Bb_o\sigma_o$, where σ_o = flow stress, and $\eta = \sqrt{[(2a/b_o)^2 + (4a/b_o) + 2]} - (2a/b_o + 1)$ [45]. Again note, K_{Im} is equivalent to an elastic fracture toughness K_{Ic}, but does not meet the overly conservative ASTM E399 size requirements. Finally, it is important to note that most tests that were not interrupted shortly beyond the maximum load, involved at least some ductile tearing. However, we have not measured initiation and resistance R-curve toughness, J_e and $J_R(da)$, as in the ASTM E1820 Standard [57]. Consistent with E1921 [49], we assume that crack initiation occurs at the maximum load, and that the corresponding load-displacement area defines the non-linear plastic K_{Jp} contribution to K_{Jm}.

To facilitate *in-situ* optical observation of the crack tip region, the fracture specimen sides were sanded with a sequence of 2000 grit SiC followed by 9μ, 3μ, and 1μ diamond lapping paper. The fracture tests were carried out at a crosshead speed of 0.04 mm/min. The pre-crack and post-test crack lengths were also measured after the specimens were broken in LN$_2$ to ensure no further ductile crack extension had occurred. Four to seven specimens were tested for each condition, except for 8x case which involved two tests per alloys.

SEM was used to observe the side and fracture surfaces of the broken specimens. Four local fracture modes, namely: W-W interparticle fracture (WW), W-cleavage (WC), W-DP interfacial debonding (WD), and DP ruptures (DR) were measured using a LIM method [27,30]. Additional details about the characterization techniques can be found elsewhere [30].

3. Results

Here we summarize the results from the fracture tests including: (a) normalized P/P_o-d plots; (b) $K_{Jm/Im}$ data; and, (c) crack tearing profiles and associated side-surface damage. Note, the normalized P/P_o-d curves are intended to facilitate inter-comparisons of the effect of specimen size and DP content, as well as to signal crack dominated fracture; they are not used to calculate toughness values.

3.1. Specimen size effects on the RT P/P_o-d and K_{Jm}/K_{Im} of the W-NiFe WHAs

Fig. 2 shows typical P/P_o-d curves for the various W contents and specimen sizes. Key P/P_o-d curve parameters and the corresponding $K_{Jm/Im}$ results are summarized in Table 1, including those previously reported for the small 1x specimens [30]. Note, not
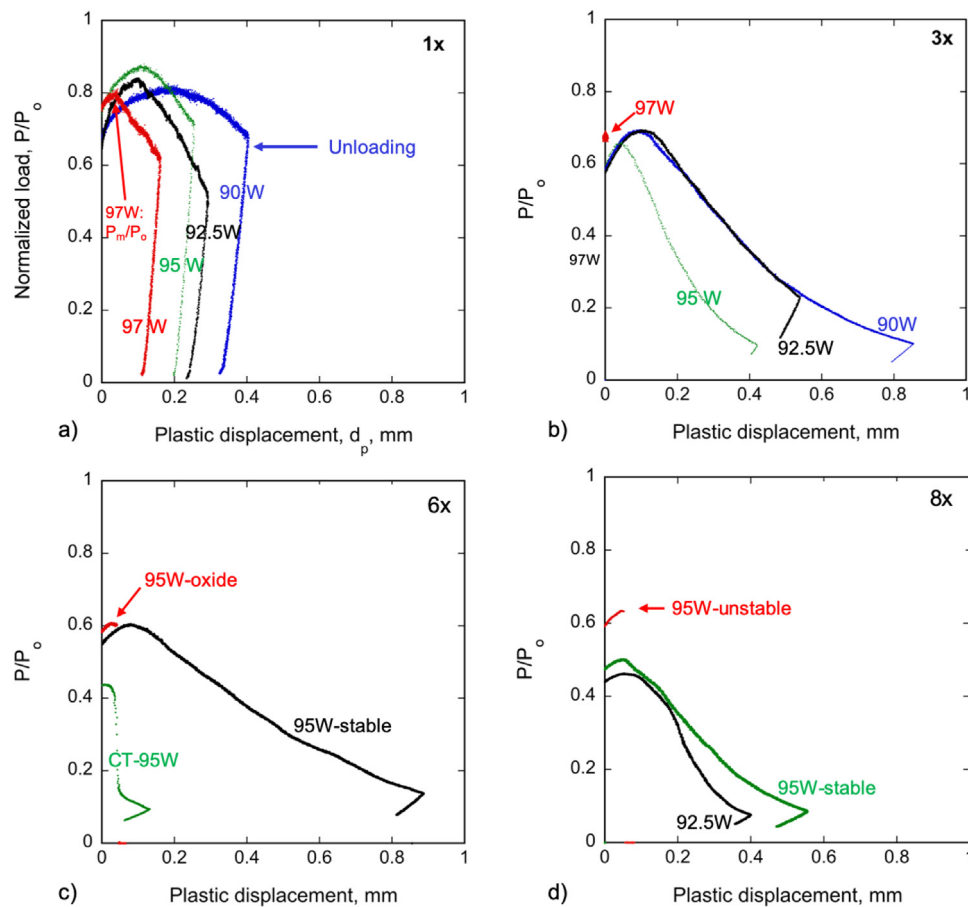
Fig. 2. The normalized load-displacement (P/P_o-d) curves for 3PB bars at RT test for (a) small, 1x; (b) 3x; (c) 6x; and, (d) 8x specimens, respectively. Note, 0.35T-CT ($\approx$ 5.5x) 95W also plotted in Fig. 2c.

Table 1
The RT K_{Im}, K_{Jp}, and K_{Jm} in MPa$\sqrt{m}$; b_o, σ_o, P/P_o at yield and maximum load with ranges, and crack propagation mode as a function of specimen size for the W-NiFe WHAs.

WHA alloy/ specimen size*	K_{Im}, MPa$\sqrt{m}$	K_{Jp}, MPa$\sqrt{m}$	K_{Jm}, MPa$\sqrt{m}$	b_o, mm	σ_o, MPa	P/P_o at yield (Range)	P/P_o at max (Range)	Crack propagation mode
90W_1x	36 ± 4	88 ± 18	97 ± 18	2.0 ± 0.2	756	0.651 ± 0.064 (0.562–0.704)	0.800 ± 0.112 (0.637– 0.892)	stable
92.5W_1x	39 ± 4	87 ± 13	96 ± 12	1.9 ± 0.1	751	0.684 ± 0.03 (0.635–0.7)	0.837 ± 0.048 (0.774 – 0.891)	stable
95W_1x	42 ± 6	102 ± 14	107 ± 14	2.0 ± 0.1	709	0.733 ± 0.018 (0.711–0.756)	0.870 ± 0.028 (0.837 – 0.904)	stable
97W_1x	36 ± 5	59 ± 14	69 ± 12	2.1 ± 0	648	0.774 ± 0.069 (0.671–0.833)	0.896 ± 0.051 (0.813–0.932)	stable
90W_3x	52 ± 2	75 ± 6	92 ± 6	5.3 ± 0.2	756	0.627 ± 0.019 (0.601–0.646)	0.689 ± 0.035 (0.658–0.736)	stable
92.5W_3x	50 ± 3	66 ± 11	83 + 11	5.2 ± 0.3	751	0.628 ± 0.031 (0.588–0.661)	0.675 ± 0.037 (0.621–0.705)	stable
95W_3x	49 ± 1	57 ± 4	75 ± 4	5.2 ± 0.2	709	0.658 ± 0.02 (0.633–0.680)	0.674 ± 0.023 (0.662 −0.715)	stable
97W_3x	38 ± 4	0 ± 0	38 ± 4	5.3 ± 0.2	648	0.586 ± 0.076 (0.502–0.684)	0.586 ± 0.076 (0.502–0.684)	unstable
95W_6x	59 ± 1	65 ± 13	89 ± 9	11±0.1	709	0.601 ± 0.008 (0.595–0.607)	0.610 ± 0.007 (0.605–0.615)	stable
95W_6x	59 ± 1	48 ± 7	76 ± 5	10±0.2	709	0.601 ± 0.001 (0.60–0.602)	0.606 ± 0.003 (0.603–0.608)	unstable (inclusions)
95W-5.5x-CT	49 ± 5	39 ± 7	63 ± 8	8.5 ± 0.2	709	0.460 ± 0.052 (0.398 −0.507)	0.461 ± 0.052 (0.399–0.510)	unstable
92.5W_8x	55 ± 3	60 ± 6	81 ± 7	15 ± 0	751	0.417 ± 0.023 (0.401–0.434)	0.445 ± 0.026 (0.426–0.463)	stable
95W_8x	60	58	82	14.9	709	0.479	0.502	stable
95W_8x	60	50	78	14.7	709	0.617	0.635	unstable

* Small, 1x: B = 1.65 mm; 3x: B = 5 mm; 6x: B = 10 mm; 8x: B = 12.7 mm. W = 2B; Span = 4 W; total length = 4.5 W.

all possible combinations of W contents and specimen size were tested.

It is important to point out the significance of K_{Im} versus K_{Jm}. Here, both correspond to the maximum load. The maximum load may occur in the elastic regime, or following non-linear plastic load deviation, generally associated with a crack blunting or a small increment of growth. K_{Jm} accounts for the additional plastic work required in the latter case. One practical implication of K_{Im} versus K_{Jm} is that fully elastic fracture can be driven by self-relieving secondary stresses, such as those due to temperature gradients. In contrast, elastic-plastic fracture work supplied by remote load displacement is needed for continuing, giving the cracked-body signaling what is equivalent to cracked -body plastic ductility.

Representative normalized plastic P/P_o-d curves for the various bend bar sizes and W content are shown in Fig. 2. Here the elastic displacement has been subtracted from the total. Fig. 2a shows a gradual post maximum load reduction in all specimens, and W contents [30] in the 1x specimen. In this case, brittle fracture is dominant, and the crack growth is minimal (~ 0.2 mm, Fig. 1a) down to the unloading point of $\sim 0.8P_m$. Notably, for the 97W the peak occurs at a lower displacement, signaling a reduction in K_{Jm} relative to the other 1x WHA specimens. The P/P_o at the initial deviation from the elastic loading line ranged from 0.526 to 0.833 (for 20 tests), averaging 0.714 ± 0.069 as shown in Table 1. The corresponding P_m/P_o ranged from 0.637 to 0.932, averaging 0.853 ± 0.071. The $P_m/P_o < 1$ signals true fracture, rather than a net section stress failure.

The corresponding normalized P/P_o-d curves for the 3x specimens are shown in Fig. 2b. All of the 90–95W WHA experienced stable crack growth down to a low P/P_o. The maximum $P_m/P_o \approx 0.661 \pm 0.062$ are lower than for the 1x specimens, as expected due to the larger crack. In contrast to the 90–95W 3x tests, the 97W alloy failed by unstable elastic fracture at a similar maximum P_m/P_o.

We selectively tested 6x (only for 95W) and 8x specimens (for 92.5 and 95W) as shown in Fig. 2c and 2d, respectively. Of the four tests for $6\times$ 95W, two showed stable crack growth, while the other two fractured unstably following a small plastic d. However, in both of these later cases, unstable fracture initiated at very large oxide inclusions (~ 1 mm x 0.7 mm) near the pre-crack tip, see Supplemental Fig. SF-1; these inclusions are the likely cause of the unstable elastic crack propagation. The 8x tests of the 95W alloy showed both stable and unstable crack growth, here with a maximum $P_m/P_o = 0.50$ (stable) and 0.64 (unstable) respectively. However, stable crack growth was observed in all the 8x 92.5W specimens tests.

Inspection of Fig. 2 shows that in the cases with stable crack growth, the range of absolute displacements at P_m, d_m, are small, but reasonably similar to each other, for the various alloys and specimen sizes. Fig. 3a shows the average absolute d_m at P_m/P_o as a function of specimen size for the 90–95W WHAs. The corresponding average displacements at $0.8P_m/P_o$, $d_{0.8}$, is also shown. In all cases, the largest difference is between the 1 and 3x specimens, while the $d_{0.8}$ decreases the most at larger sizes (Fig. 3a). Fig. 3b plots the average 90–95W P_m/P_o versus the square-root of initial crack length, $\sqrt{a_i}$, for all the specimen sizes. In the cases investigated here, size has a weak effect on the absolute displacement required for fracture, especially for 3x to 8x specimens. Note, the displacement can also be normalized by dividing by the bend bar span (S). The resulting dimensionally equivalent stain decreases slightly faster than 1/S.

The specimen geometry also affected the WHA fracture behavior, as shown in Fig. 2c. The 5.5x 95W CT P_m/P_o is lower than for the bend bar and unstable crack extension occurs after a small increment of plastic displacement. However, the crack arrests after a

large pop-in, and grows a small increment before the final unloading.

The corresponding trends in the K_{Jm} and K_{Im} are shown in Fig. 4a, and 4b, respectively. The K_{Jm} for the 1x specimens, averages 100 ± 15 MPa$\sqrt{m}$ for 90–95W, while dropping to $\approx 69 \pm 12$ MPa$\sqrt{m}$ at 97W. Fig. 4a also shows the average K_{Jm} of the 3x specimen decreases between 90 and 95W from 92 to 72 MPa$\sqrt{m}$, averaging 83.3 ± 8.5 MPa$\sqrt{m}$. The 3x toughness again experiences a large decrease at 97W, to an elastic $K_{Im} \approx 38 \pm 4$ MPa$\sqrt{m}$. Again, however, this is still ≈ 4.75 times higher than that for typical monolithic W ($\approx 8 \pm 4$ MPa$\sqrt{m}$). The corresponding average toughness for stable versus inclusion initiated unstable crack growth for the 6x 95W are $K_{Jm} \approx 89 \pm 9$ and $\approx 76 \pm 5$ MPa$\sqrt{m}$, respectively, averaging 82.6 ± 9.5 MPa$\sqrt{m}$. Both 8x 92.5W and one of 95W WHA tests showed stable crack growth, while another 8x 95W test experienced unstable crack growth, with only a small plastic J_p contribution. The average of the 8x $K_{Jm} = 80.5 \pm 4.1$ MPa$\sqrt{m}$. Thus, the overall K_{Jm} averages for 90–95% W alloys were 83.3 (3x), 82.6 (6x) and 80.5 (8x) MPa$\sqrt{m}$; these small differences are well within expected data scatter.

In all but one case (3x 97W), the WHA experienced elastic-plastic fracture, again where the elastic K_{Im} contribution to K_{Jm} was evaluated at the maximum load. As shown in Table 1 and Fig. 4b, in contrast to K_{Jp}, the 90–95W K_{Im}, increased with increasing specimen size. With one exception, the K_{Im} were similar for the same size of various W contents, averaging: 1x 37 ± 3; 3x 50 ± 3; 6–8x 59 ± 2 MPa$\sqrt{m}$. The exception was the K_{Im} for 3x 97W specimens, which only increased from 34 ± 2 for the 1x to 38 ± 4 for the 3x tests. The 3x 97W fracture was fully elastic, with $K_{Jp} = 0$. Note, the required ligament size for ASTM E399 [58] of $2.5(K_{Im}/\sigma_y)^2$ is ≈ 10.1 mm for 3x 97W test, which is slightly larger than the specimen $b_o \sim 5.3 \pm 0.2$ mm. However, it is well known that E399 is overly conservative in that SSY field can persist well beyond the fully elastic limit as fully recognized by elastic-plastic fracture mechanics [45].

A representative P/P_o-d curve for the CT test is shown in Fig. 2c, and the average K_{Jm} values are summarized and plotted in Table 1 and Fig. 4a, respectively. All four CT specimens tested at RT experienced only slight deviations from the elastic loading line that contributed only a small increment of J_p. Both the average K_{Im} and K_{Jm} for 95W 5.5x CT, are lower than the $6\times$ 95W 3PB tests. The CT test $K_{Im} = 49 \pm 6$ MPa$\sqrt{m}$ and $K_{Jm} = 63 \pm 8$ MPa$\sqrt{m}$, compared to $K_{Im} = 61 \pm 0.5$ and $K_{Jm} = 89 \pm 9$ MPa$\sqrt{m}$ for 3PB tests with stable crack growth, and $K_{Im} = 59 \pm 0$ MPa$\sqrt{m}$ and $K_{Jm} = 76 \pm 4$ MPa$\sqrt{m}$ for the inclusion associated unstable crack growth cases (see Table 1). The lower plastic contribution to K_{Jm} in the CT test is, again, due to unstable fracture with the immediate onset of crack growth following a small deviation from the elastic loading line. A full analysis of CT versus 3PB test crack stability would require a R-curve measurement, which is beyond the scope of this paper.

Summarizing key fracture toughness test observations, the K_{Jm} for the 1x tests are higher than for the larger specimens, indicating some size effect. Stable crack growth occurred in all the WHA 1x and 3x tests, except the $3\times$ 97W specimens fractured elastically. Elastic-plastic fracture with crack blunting, or some stable crack growth, occurred in seventeen of the twenty 3 to $8\times$ 90 to 95W tests, shown as unfilled symbols in Fig. 4a, with an average $K_{Jm} = 83 \pm 8$ MPa$\sqrt{m}$. The corresponding average $K_{Jm} = 77 \pm 3$ MPa$\sqrt{m}$, was only slightly lower in the larger specimen tests with nearly elastic unstable crack growth, even those with large inclusions. A modest decrease in K_{Jm} with increasing W was observed only in the 3x tests, while this trend was not found in the 6 and 8x specimens. These results suggest that ≈ 5 wt% NiFe DP additions are enough to assure high WHA toughness unirradi-
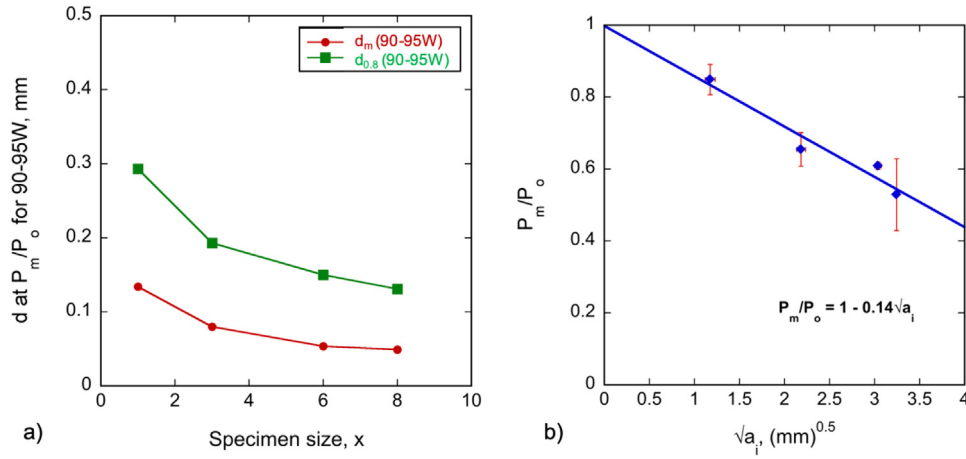
Fig. 3. Plots show for the 90–95W WHAs: (a) absolute displacement, d at the maximum load, P_m/P_o and at 80% of post maximum load, $0.8P_m/P_o$ as a function of specimen size, x; and, (b) average P_m/P_o versus square-root of initial crack length, $\sqrt{a_i}$, for all the specimen sizes.
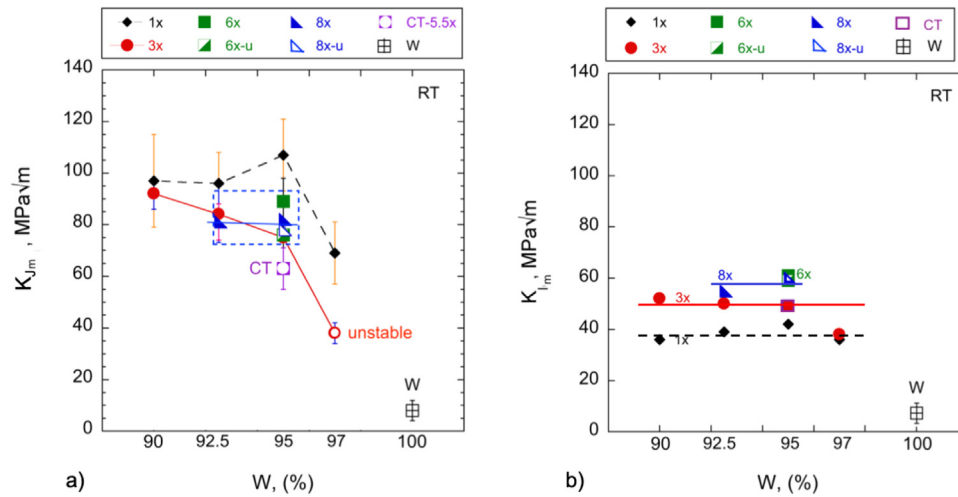

Fig. 4. The RT: a) elastic-plastic (K_{Jm}), and b) elastic (K_{Im}) fracture toughness in MPa$\sqrt{m}$ as a function of specimen size, geometry and alloy compositions. Filled and unfilled symbols represent stable and unstable (u) crack propagation, respectively.

ated RT toughness without compromising low-level waste disposal limit [32,59].

3.2. Crack propagation and toughening mechanisms

Representative side-view SEM images for 1× 90W and 97W in Fig. 5a and b, respectively, shows stable crack growth, accompanied by extensive microcracking. Fig. 5c shows stable crack growth in the 3× 90W alloy test, again with extensive microcracking. In contrast, Fig. 5d shows that elastic fracture with a single, unstable macro-crack occurs in the 3x test of a 97W alloy.

Similar crack propagation and microcracking patterns were observed in the other cases of stable versus unstable crack growth (see Fig. 5a–d and supplemental Figs. SF-2, SF-3, SF-4, and SF-5). The fractographs in SF-5a for 1x 90W shows crack initiation is dominated by WC microcracks, which are initially stabilized by ductile phase (DP), but later propagate when the DP ruptures and the coplanar WC microcracks coalescence. SF-5b-e show the similar evidence for the 95W 1x to 8x tests with stable crack growth, respectively. SF-5f shows unstable elastic fracture of 3x 97W which is WC-dominated.

The homogeneity of in-and-between WHA plates is also an issue as illustrated in Fig. 6. For example, variations from 13% to 22%

for the 90W and 6 to 9% for the 97W are observed in the plates, respectively (Fig. 6). The 95W 6x specimens were fabricated from a second WHA plate. Note, for the two elastically fractured 6x 95W alloys, very large oxide inclusions (∼1 mm x 0.7 mm), located near the pre-crack tip, were likely the cause of the unstable crack propagation (supplemental Fig. SF-1). DP area fraction (DP_f) of all specimens' sizes were selectively sampled, although the measurements were made some distance from the crack propagation plane, and may vary due to inhomogeneities. The DP_f values (6.3 ± 1.4) for the unstable 6x 95W tested specimens are lower than the average of ≈ 11% for the same 95W plate (see Table 2 in Ref. [30], and ST-1). Nevertheless, as shown in Fig. 7, similar higher K_{Jm} were observed in all cases for the 3–8x tests for $DP_f > 8\%$ (Supplemental Table ST-1, and Fig. 7). The average K_{Jm} is lower and more scattered for DP_f between 6 and 8% DP. Along with a lower DP_f, some locations in the 8x specimens, from the second 95W plate, had weak, or a nearly absent, bonding between W-particles and DP (SF-4d); which may contribute to nearly elastic fracture. This points to the importance of developing WHA fabrication paths that result in uniform microstructures and properties. Inclusion initiation sites could also add a statistical component to size effects, as is the case in steels [47]. However, as discussed below, statistical size effects are not apparent in the limited data in this study. Lo-
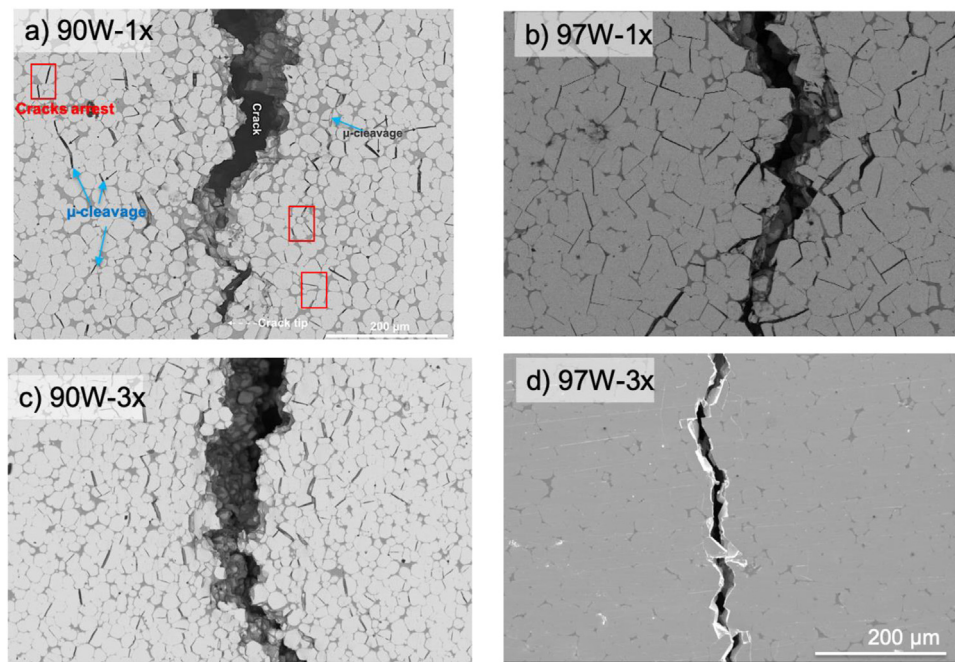
Fig. 5. Side surface crack propagation mode along with damage profile for: (a) 1× 90W; (b) 1× 97W; (c) 3× 90W; and, (d) 3× 97W WHA specimens, respectively. The scale bar is 200 μm for all, shown in Fig. d.
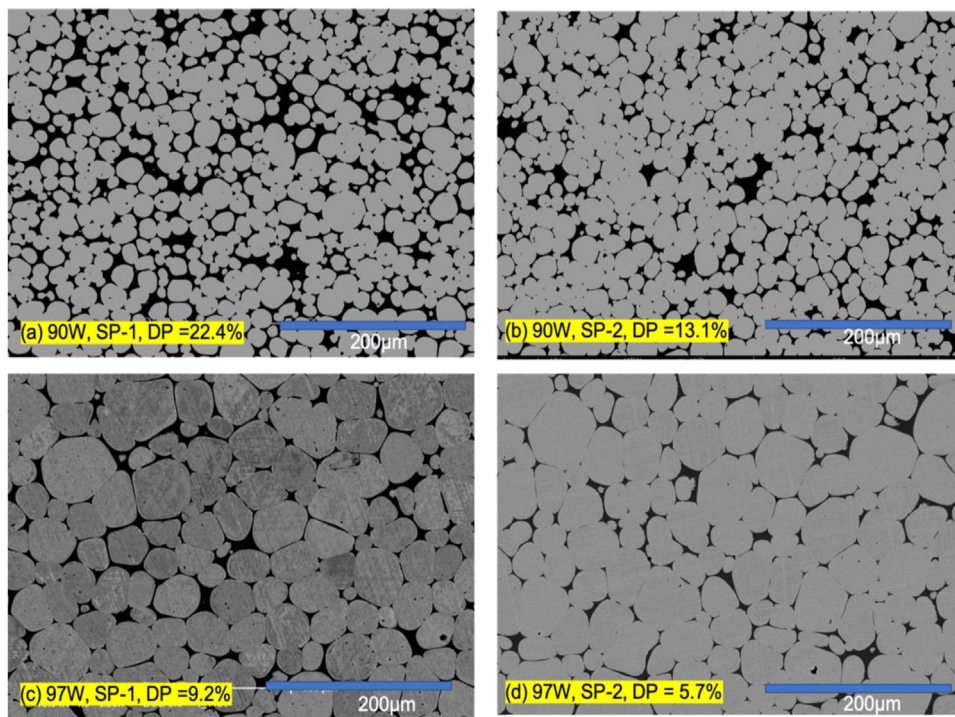

Fig. 6. Backscattered SEM images showing local microstructural variations prepared from two different specimens of the same plate for: (a,b) 90W, and (c,d) 97W-NiFe alloys, respectively.

cal damage modes and the role of W-cleavage on WHA toughness are discussed further in the Supplemental Discussion Section (SD-1) along with Supplemental Figs. SF-6 and SF-7, and Supplemental Table ST-2.

All of the 0.35T-CT ($\approx$ 5.5x) 95W specimens, which were also fabricated from the second plate, experienced unstable crack propagation after reaching the maximum load, with lower K_{Jm} compared to the 3PB 95W 6x specimens (Table 1, and Fig. 2c). Only limited microcracking was observed in the CT tests, and the over-

all microcracked zone was much smaller than the 95W 3PB tests (SF-4e,f). Again, a lower DP_f, combined with locations weak or absent W-DP interfacial bonding (supplemental Fig. SF-4d) may have reduced K_{Jm} and promote unstable crack growth.

4. Deformation limits for avoiding size effects and discussion

Size effects on RT K_{Jm} are clearly observed only between the 1x and larger 3–8x tests, with $K_{Jm}(1x)/K_{Jm}(3x)$ decreasing with de-
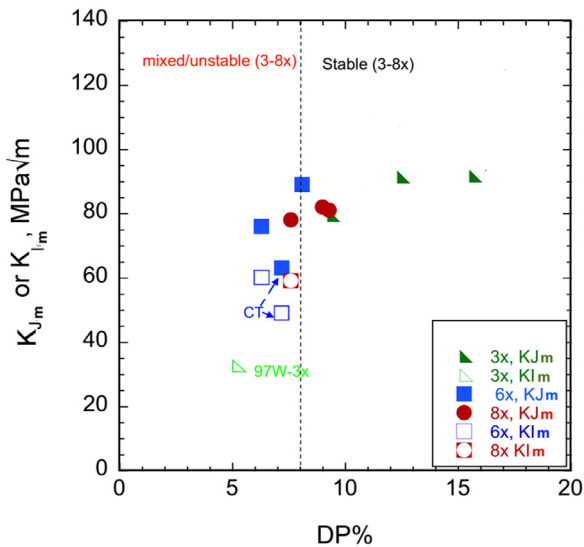
Fig. 7. The measured DP_f area % vs. RT toughness for WHAs.

creasing W as: 1.8 (97W), 1.4 (95W). 1.15 (92.5W) and 1.05 (90W). Note, 3x fracture of the 97W is elastic with $K_{Jm} = K_{Im}$. This is in part due to decreases in $K_{Jm/Im}$ with increasing W in the 3x tests. Systematic size effects are not observed in the larger specimens up to 95W.

As discussed in the Introduction, size effects on cleavage fracture in steels arise from both: (a) loss of triaxial constraint, reducing blunting crack tip stress concentrations; and, (b) weakest link statistical effects associated with variations in highly stressed volumes that depend on the crack front length [47,48]. The limits needed to avoid deformation-related size effects can be expressed in terms of a total elastic-plastic J_{lim}, as $J_{lim} = b_o\sigma_o/M$, where σ_o is flow stress. Fig. 8 plots K_{Im}, K_{Jp} and K_{Jm} versus the J-based constraint deformation metric $M = b_o\sigma_o/J_m$. The average M for 1x specimen, which is 85 ± 28, increases with specimen size up to $\approx 728 \pm 19$ for the 8x specimens. The measured K_{Im} increase between 1x and larger sizes, except for the 97W alloy, while the plastic K_{Jp} slightly decreases (Table 1). The corresponding K_{Im} and K_{Jm} for the larger specimens, with $M \geq 200$, are approximately constant, while K_{Jp} also decreases slightly. Note, however, all the toughness variations at and above 3x are within the data scatter. Therefore, it appears that $M = 200$ provides a reasonable
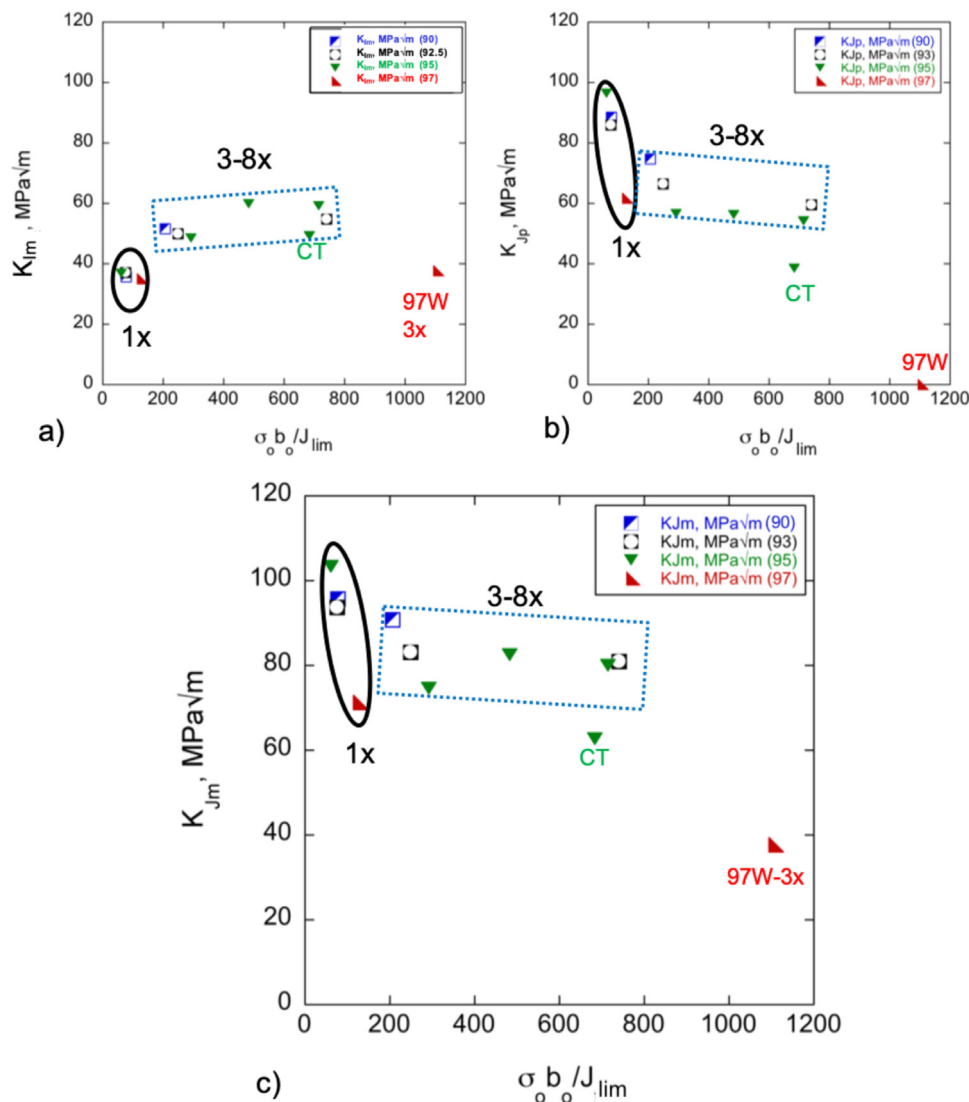

Fig. 8. The K_{Im}, K_{Jp} and K_{Jm} values vs. $M = b_o\sigma_o/J_{lim}$ are plotted in: (a); (b); and, (c), respectively.

condition to avoiding constraint loss size effects. Only the K_{Jm} (69–107 MPa$\sqrt{m}$) for 1x specimens were higher than the corresponding K_{Jlim} values (46 MPa$\sqrt{m}$) for M = 200 among all of the alloys and tests.

Plane strain size effects on ductile fracture initiation are less severe than for cleavage [45,47,57]. Indeed, the ASTM E1820 M = 10 for ductile tearing J_c, is generally thought to be sufficient to avoid constraint loss effects [57]. However, M = 200 appears to be needed for ductile tearing in WHA.

The ASTM E1921 cleavage standard also accounts for the statistical effect of the crack front length on the measured K_{Jm}. Longer crack fronts increase the probability of the concentrated crack tip stress fields triggering a cleavage event, which is controlled by weakest link statistics [46,47]. There is not a priori reason to assume that some variant of such statistic effects might play a role in WHA fracture. The ASTM E1921 statistical size effect is described by

$$K_{Jm}(B_1) = \left[K_{Jm}(B_2) - 20 \right] [B_2/B_1]^{1/4} + 20 \left(MPa\sqrt{m} \right)$$

Here B_1 and B_2 are the specimen thickness dimension. Assuming $K_{Jm}(3x) = 83$ MPa$\sqrt{m}$, the statistical specimen dimension size adjustment would predict $K_{Jm}(8x) = 69.3$ MPa$\sqrt{m}$. Clearly, the limited data in this study are not consistent with the predicted ASTM E1921 statistical size effect.

5. Conclusions

The effect of various specimen sizes on the room temperature fracture toughness for the WNiFe WHA has been conducted. The key results and conclusions can be summarized as follows:

- Significant and systematic specimen size effects on elastic-plastic fracture toughness, K_{Jm}, are only observed in the 1x and 3x 97W tests.
- There are relatively weak competing trends in the elastic and plastic contributions of the K_{Jm}, which increase and decrease, respectively, in larger specimens.
- The post elastic displacements and ductile tearing weakly decrease with specimen size.
- Statistical, highly stressed volume size effects, which are important in steels, are weak or absent in WHA.
- A constraint limit $M \geq 200$ appears to be sufficient to avoid size effects in 90–95W alloys.
- The overall results of this study suggest that 95W alloys may be an optimal choice for fusion divertor applications.
- The K_{Jm} are significantly lower in CT tests than for similarly sized 3PB specimens. However, this in part may be due to lower DP fractions (DP_f) in this 95W alloy plate.
- The quality of the composite and local variations in the DP_f, which varies within and between WHA plates, plays a role and may confound interpretation of size and geometry effects in some cases, and suggest a good, uniform DP-W-particle bonding and a minimum $DP_f = 8\%$ may be needed as a quality assurance metric.

Declaration of Competing Interest

The authors declare that they have no known competing financial interests or personal relationships that could have appeared to influence the work reported in this paper.

CRediT authorship contribution statement

M.E. Alam: Formal analysis, Data curation, Investigation, Methodology, Writing – original draft, Writing – review & edit-

ing. **G.R. Odette:** Supervision, Conceptualization, Funding acquisition, Project administration, Writing – review & editing.

Supplementary materials

Supplementary material associated with this article can be found, in the online version, at doi:10.1016/j.jnucmat.2022.154025.

References

[1] M. Rieth, S.L. Dudarev, S.M.G. De Vicente, et al., Recent progress in research on tungsten materials for nuclear fusion applications in Europe, J. Nucl. Mater. 432 (2013) 482–500.

[2] P. Norajitra, R. Giniyatulin, W. Krauss, V. Kuznetsov, I. Mazul, I. Ovchinnikov, J. Reiser, M. Rieth, V. Widak, Current status of He-cooled divertor development for DEMO, Fusion Eng. Des. 84 (2009) 1429–1433.

[3] V. Philipps, Tungsten as material for plasma-facing components in fusion devices, J. Nucl. Mater. 415 (2011) S2–S9.

[4] J. Davis, V. Barabash, A. Makhankov, L. Plöchl, K. Slattery, Assessment of tungsten for use in the ITER plasma facing components, J. Nucl. Mater. 258–263 (1998) 308–312.

[5] E. Gaganidze, A. Chauhan, H.C. Schneider, D. Terentyev, G. Borghmans, J. Aktaa, Fracture-mechanical properties of neutron irradiated ITER specification tungsten, J. Nucl. Mater. 547 (2021) 152761.

[6] Jr C. Henager, W. Setyawan, T. Roosendaal, N. Overman, B. Borlaug, E. Stevens, K. Wagner, R. Kurtz, G.R. Odette, B. Nguyen, K. Cunningham, Ductile-phase toughened tungsten for plasma-facing materials in fusion reactors, Int. J. Powder Metall. 53 (2017) 53–69.

[7] J. Reiser, J. Hoffmann, U. Jäntsch, M. Klimenkov, S. Bonk, C. Bonnekoh, M. Rieth, A. Hoffmann, T. Mrotzek, Ductilisation of tungsten (W): on the shift of the brittle-to-ductile transition (BDT) to lower temperatures through cold rolling, Int. J. Refract. Met. Hard Mater. 54 (2016) 351–369.

[8] B. Gludovatz, S. Wurster, A. Hoffmann, R. Pippan, Fracture toughness of polycrystalline tungsten alloys, Int. J. Refract. Met. Hard Mater. 28 (2010) 674–678.

[9] K.T.V. Rao, G.R. Odette, R.O. Ritchie, Ductile-reinforcement toughening in γ-TiAl intermetallic-matrix composites: effects on fracture toughness and fatigue-crack propagation resistance, Acta Metall. Mater. 42 (1994) 893–911.

[10] G.R. Odette, B.L. Chao, J.W. Sheckherd, G.E. Lucas, Ductile phase toughening mechanisms in a TiAl-TiNb laminate composite, Acta Metall. Mater. 40 (1992) 2381–2389.

[11] M.G. Mendiratta, J.J. Lewandowski, D.M. Dimiduk, Strength and ductile-phase toughening in the two-phase Nb/Nb$_5$Si$_3$ alloys, Metall. Trans. A 22 (1991) 1573–1583.

[12] L.S. Sigl, P.A. Mataga, B.J. Dalgleish, R.M. McMeeking, A.G. Evans, On the toughness of brittle materials reinforced with a ductile phase, Acta Metall. 36 (1988) 945–953.

[13] D.V. Edmonds, P.N. Jones, Interfacial embrittlement in liquid-phase sintered tungsten heavy alloys, Metall. Trans. A 10 (1979) 289–295.

[14] B.C. Muddle, Interphase boundary precipitation in liquid phase sintered W-Ni-Fe and W-Ni-Cu alloys, Metall. Trans. A 15 (1984) 1089–1098.

[15] R. German, J. Hanafee, S. DiGiallonardo, Toughness variation with test temperature and cooling rate for liquid phase sintered W-3.5Ni-1.5Fe, Metall. Trans. A 15 (1984) 121–128.

[16] K.S. Churn, R.M. German, Fracture behavior of W-Ni-Fe heavy alloys, Metall. Trans. A Phys. Metall. Mater. Sci. 15 (A) (1984) 331–338.

[17] D.V. Edmonds, Structure/property relationships in sintering heavy alloys, Refract. Met. Hard Mater. 10 (1991) 15–26.

[18] R.M. German, A. Bose, S.S. Mani, Sintering time and atmosphere influences on the microstructure and mechanical properties of tungsten heavy alloys, Metall. Trans. A 23 (1992) 211–219.

[19] K.M.O. Zamora, J.G. Sevillano, M.F. Perez, Fracture toughness of W heavy metal alloys, Mater. Sci. Eng. A 157 (1992) 151–160.

[20] A. Upadhyaya, Processing strategy for consolidating tungsten heavy alloys for ordnance applications, Mater. Chem. Phys. 67 (2001) 101–110.

[21] Z.H. Zhang, F.C. Wang, S.K. Li, L. Wang, Deformation characteristics of the 93W-4.9Ni-2.1Fe tungsten heavy alloy deformed by hydrostatic extrusion, Mater. Sci. Eng. A 435-436 (2006) 632–637.

[22] S. Islam, X. Qu, X. He, Investigation of composition and microstructure effect on fracture behaviour of tungsten heavy alloys, Powder Metall. 50 (2007) 11–13.

[23] A. Mondal, D. Agrawal, A. Upadhyaya, Microwave sintering of refractory metals/alloys: W, Mo, Re, W-Cu, W-Ni-Cu and W-Ni-Fe alloys, J. Microw. Power Electromagn. Energy 44 (2010) 28–44.

[24] Z.A. Hamid, S.F. Moustafa, W.M. Daoush, F.A. Mouez, M. Hassan, Fabrication and characterization of tungsten heavy alloys using chemical reduction and mechanical alloying methods, Open J. Appl. Sci. 03 (2013) 15–27.

[25] M. Scapin, Mechanical characterization and modeling of the heavy tungsten alloy IT180, Int. J. Refract. Met. Hard Mater. 50 (2015) 258–268.

[26] X. Gong, J. Fan, F. Ding, Tensile mechanical properties and fracture behavior of tungsten heavy alloys at 25-1100°C, Mater. Sci. Eng. A 646 (2015) 315–321.

[27] K. Hu, X. Li, X. Ai, S. Qu, Y. Li, Fabrication, characterization, and mechanical properties of 93W-4.9Ni-2.1Fe/95W-2.8Ni-1.2Fe/95W-2.8Ni-1.2Fe-1Al$_2$O$_3$ heavy alloy composites, Mater. Sci. Eng. A 636 (2015) 452–458.

[28] U.R. Kiran, A. Panchal, M. Sankaranarayana, G.V.S.N. Rao, T.K. Nandy, Effect of alloying addition and microstructural parameters on mechanical properties of 93% tungsten heavy alloys, Mater. Sci. Eng. A 640 (2015) 82–90.

[29] M.B. Shongwe, S. Diouf, M.O. Durowoju, P.A. Olubambi, M.M. Ramakokovhu, B.A. Obadele, A comparative study of spark plasma sintering and hybrid spark plasma sintering of 93W-4.9Ni-2.1Fe heavy alloy, Int. J. Refract. Met. Hard Mater. 55 (2016) 16–23.

[30] M.E. Alam, G.R. Odette, On the remarkable fracture toughness of 90 to 97W-NiFe alloys revealing powerful new ductile phase toughening mechanisms, Acta Mater. 186 (2020) 324–340.

[31] G.R. Odette, M.E. Alam, K. Cunningham, Ductile-phase toughened tungsten for plasma facing materials, Final Report, DOE-UCSB-ER54275, United States (2019) 1-152.

[32] M.E. Alam, J. Wang, C.H. Henager, W. Setyawan, G.R. Odette, The effect of hot rolling on the strength and fracture toughness of 90W–7Ni3Fe tungsten heavy metal alloys, Mater. Sci. Eng. A 824 (2021) 141738.

[33] R. Neu, H. Maier, M. Balden, R. Dux, S. Elgeti, H. Gietl, H. Greuner, A. Herrmann, T. Höschen, M. Li, V. Rohde, D. Ruprecht, B. Sieglin, I. Zammuto, Results on the use of tungsten heavy alloys in the divertor of ASDEX Upgrade, J. Nucl. Mater. 511 (2018) 567–573.

[34] Q. An, A. Elshafiey, L. Huang, D.A. Hammer, M. Hassani, Plasma and X-ray radiation-induced damage mechanisms in a tungsten heavy alloy, J. Nucl. Mater. 539 (2020) 152325.

[35] T. Laas, K. Laas, J. Paju, J. Priimets, S. Tõkke, B. Väli, V. Shirokova, M. Antonov, V.A. Gribkov, E.V. Demina, V.N. Pimenov, M. Paduch, R. Matulka, M. Akel, Behaviour of tungsten alloy with iron and nickel under repeated high temperature plasma pulses, Fusion Eng. Des. 151 (2020) 111408.

[36] Y. Şahin, Recent progress in processing of tungsten heavy alloys, J. Powder Technol. 2014 (2014) 1–22.

[37] W.D. Cai, Y. L, R.J. Dowding, F.A. Mohamed, E.J. Lavernia, A review of tungsten-based alloys as kinetic energy penetrator materials, Rev. Mater. 3 (1995) 71–131.

[38] A.A.N. Németh, J. Reiser, D.E.J. Armstrong, M. Rieth, The nature of the brittle–to-ductile transition of ultra fine grained tungsten (W) foil, Int. J. Refract. Met. Hard Mater. 50 (2015) 9–15.

[39] J.H. You, Design feasibility study of a divertor component reinforced with fibrous metal matrix composite laminate, J. Nucl. Mater. 336 (2005) 97–109.

[40] J. Riesch, Y. Han, J. Almanstötter, J.W. Coenen, T. Höschen, B. Jasper, P. Zhao, C. Linsmeier, R. Neu, Development of tungsten fibre-reinforced tungsten composites towards their use in DEMO - Potassium doped tungsten wire, Phys. Scr. T167 (2016) 14006.

[41] M. Rühle, A.G. Evans, R.M. McMeeking, P.G. Charalambides, J.W. Hutchinson, Microcrack toughening in alumina/zirconia, Acta Metall. 35 (1987) 2701–2710.

[42] A.G. Evans, Z.B. Ahmad, D.G. Gilbert, P.W.R. Beaumont, Mechanisms of toughening in rubber toughened polymers, Acta Metall. 34 (1986) 79–87.

[43] A.G. Evans, R.M. Cannon, Toughening of brittle solids by martensitic transformations, Acta Metall. 34 (1986) 761–800.

[44] J.W. Hutchinson, Non-linear Fracture Mechanics, Technical University of Denmark, 1979.

[45] T.L. Anderson, Fracture Mechanics: Fundamentals and Applications, 3rd ed., Taylor & Francis Group, FL, USA, 2005.

[46] G.R. Odette, H.J. Rathbun, M. Hribernik, T. Yamamoto, M. He, P. Spätig, V. Ghetta, D. Gorse, D. Mazière, V. Pontikis, A multiscale approach to measuring and modeling cleavage fracture toughness in structural steels, in: Materials Issues Generation IV Systems, Springer Netherlands, Dordrecht, 2008, pp. 203–226.

[47] H.J. Rathbun, G.R. Odette, M.Y. He, T. Yamamoto, Influence of statistical and constraint loss size effects on cleavage fracture toughness in the transition–A model based analysis, Eng. Fract. Mech. 73 (2006) 2723–2747.

[48] H.J. Rathbun, G.R. Odette, T. Yamamoto, G.E. Lucas, Influence of statistical and constraint loss size effects on cleavage fracture toughness in the transition – a single variable experiment and database, Eng. Fract. Mech. 73 (2006) 134–1158.

[49] ASTM E1921-20, Standard test method for determination of reference temperature, to, for ferritic steels in the transition range, in: Annual Book ASTM Standards,, ASTM International, 2020, pp. 1–25. 100 Barr Harbor Drive, PO Box C700, West Conshohocken, PA 19428-2959, United States.

[50] G.R. Odette, E. Stergar, D. Gragg, K. Fields, J. Heathcote, C.H. Henager, R.J. Kurt, W-alloy and composite fracture test method development and initial exploration of ductile phase toughening, Fusion Reactor Materials Program Semiannual Progress Report DOE0313/52, 52 (2012) 89–102.

[51] T. Anderson, R. Dodds, Specimen size requirements for fracture toughness testing in the transition region, J. Test. Eval. 19 (1991) 123–134.

[52] K. Wallin, The size effect in KIC results, Eng. Fract. Mech. 22 (1985) 149–163.

[53] J.R. Rice, D.M. Tracey, On the ductile enlargement of voids in triaxial stress fields, J. Mech. Phys. Solids 17 (1969) 201–217.

[54] R.L. Tregoning, J.A. Joyce, To evaluation in common specimen geometries. Applications of fracture mechanics in failure assessment, ASME Publ. PVP 412 (2000) 143–152.

[55] M.E. Alam, G.R. Odette, On the effect of specimen size, geometry and ductile phase content on the fracture toughness of tungsten heavy metal alloys, DOE Fusion React. Mater. Progr. Semiannu. Prog. Rep. DOE0313/66, 66 (2019) 45–52.

[56] J.R. Davis, Properties and Selection: Nonferrous Alloys and Special-Purpose Materials, 10th ed., ASM Handbook, ASM, Metal Park, Ohio, 1993.

[57] ASTM E1820-13, Standard test method for measurement of fracture toughness, in: ASTM Book of Standards, ASTM International, West Conshohocken, PA, United States, 2013, pp. 1–54.

[58] ASTM E399, Standard test method for linear-elastic plane-strain fracture toughness k1c of metallic material, in: Annual Book ASTM Standard, ASTM International, West Conshohocken, PA, United States, 2013, pp. 1–33.

[59] Jr L.A. El-Guebaly, W. Setyawan, C.H. Henager, R.J. Kurtz, G.R. Odette, Neutron activation and radiation damage assessment for W-Ni-Fe tungsten heavy alloys with variable Ni content, Nucl. Mater. Energy 29 (2021) 101092.